The Astrophysical Journal, 917:62 (9pp), 2021 August 20 https://doi.org/10.3847/1538-4357/ac09ed

Characterization of HD 206893 B from Near- to Thermal-infrared

Tiffany Meshkat[1], Peter Gao[2,9], Eve J. Lee[3], Dimitri Mawet[4,5], Elodie Choquet[6], Marie Ygouf[5], Rahul Patel[1], Garreth Ruane[5], Jason Wang[4,10], Nicole Wallack[7], Olivier Absil[8,11], and Charles Beichman[1,5]
[1] IPAC, California Institute of Technology, M/C 100-22, 1200 East California Boulevard, Pasadena, CA 91125, USA
[2] Department of Astronomy and Astrophysics, University of California, Santa Cruz, Santa Cruz, CA 95064, USA
[3] Department of Physics and McGill Space Institute, McGill University, 3550 rue University, Montreal, QC H3A 2T8, Canada
[4] Department of Astronomy, California Institute of Technology, 1200 East California Boulevard, Pasadena, CA 91125, USA
[5] Jet Propulsion Laboratory, California Institute of Technology, 4800 Oak Grove Drive, Pasadena, CA 91109, USA
[6] Aix Marseille Univ, CNRS, CNES, LAM, Marseille, France
[7] Division of Geological & Planetary Sciences, California Institute of Technology, Pasadena, CA 91125, USA
[8] Space sciences, Technologies, and Astrophysics Research (STAR) Institute, Université de Liège, 19c allée du Six Août, B-4000 Sart Tilman, Belgium
Received 2020 December 7; revised 2021 June 5; accepted 2021 June 8; published 2021 August 17

Abstract

HD 206893 B is a brown-dwarf companion orbiting inside the debris disk of its host star. We detect the brown dwarf in the *Ms* band using the Keck/NIRC2 instrument and vortex coronagraph. We measure its magnitude to be $Ms = 12.97^{0.10}_{-0.11}$. It is at an angular separation of $0\farcs22 \pm 0\farcs03$, and a position angle of $39.6° \pm 5.4°$ east of north. Using this *Ms*-band measurement and the system age, we use three evolutionary models to estimate the mass to be 12–78 $M_{\rm Jup}$. We analyze the atmospheric properties from 1–5 μm using a grid of simulated atmospheric models. We find that a sedimentation flux $f_{\rm sed}$ value ~0.2 provides the best fit to the data, suggesting high vertically extended clouds. This may be indicative of high-altitude grains or a circumplanetary disk. Our model radii and luminosities for the companion find the best fits are ages of <100 Myr and masses <20 $M_{\rm Jup}$, consistent with our mass estimate from the evolutionary models using the *Ms*-band data alone. We detect orbital motion of the brown dwarf around the host star in comparison to the discovery image and derive orbital parameters. Finally we analyze how the companion brown dwarf interacts with the debris disk by estimating the location of the chaotic zone around the brown dwarf using values derived from this study's estimated mass and orbital constraints. We find that the collisions within the debris belt are likely driven by secular perturbations from the brown dwarf, rather than self-stirring.

Unified Astronomy Thesaurus concepts: Brown dwarfs (185); Debris disks (363); Direct imaging (387); Coronagraphic imaging (313); Astrometry (80); Exoplanet atmospheres (487)

1. Introduction

HD 206893 is a bright ($H = 5.69$), nearby (40.77 ± 0.05 pc; Gaia EDR3), F5V star with an unresolved debris disk, inferred by its infrared excess (Moór et al. 2006). Milli et al. (2017) reported the detection of a low-mass companion at a projected separation of ~10 au, inside the debris-disk belt with an inner edge of ~50 au. The companion was first detected in the *H* band with infrared dual-band imager and spectrograph (IRDIS) on Spectro-Polarimetric High-contrast Exoplanet REsearch (SPHERE)/Very Large Telescope (VLT), with $H = 16.79 \pm 0.06$ mag. The team confirmed the companion is comoving with follow-up NAOS-CONICA (NACO)/VLT observations in the L' band and found a magnitude of $13.43^{+0.17}_{-0.15}$. The age for the star is not well constrained, as it is not a member of a moving group. The age ranges from 200 Myr (Zuckerman & Song 2004) up to 2.1 Gyr (David et al. 2016). Using the AMES-Cond model (Baraffe et al. 2003) and the assumed system age range of 0.2–2 Gyr, Milli et al. (2017) found the mass of the companion to be 24–75 $M_{\rm Jup}$. In comparison to young bound and field companions, they found that HD 206893 B is one of the reddest late-L dwarfs, likely due to a dusty atmosphere. They concluded that the companion is likely orbiting interior to and in the same plane as the debris disk. This is only the second brown-dwarf companion discovered inside a debris-disk gap, following the discovery of HR 2562 B (Konopacky et al. 2016).

Delorme et al. (2017) characterized the companion with spectral data from the integral field spectrograph (IFS) on SPHERE/VLT, providing spectral coverage from 0.95–1.63 μm with a resolution of $R = 30$. These observations were obtained in dual-band imaging, thus K1- (2.110 μm) and K2-band (2.251 μm) imaging data were simultaneously obtained with the IFS data. Using a range of age identifiers applied to derive the host star properties (color–magnitude position, lithium and barium abundances, rotation rate, X-ray, chromospheric emission, and potential moving-group association), they adopted the age of 250^{+450}_{-200} Myr. The error on the age of the star is large because the slow spin-down of mid-F stars onto the main sequence leads to ambiguity in age. They compared the spectral energy distribution (SED) of the companion to a grid of BT-Settl (Allard 2014) models as well as Exoplanet Radiative-convective Equilibrium Model (Exo-REM; Baudino et al. 2015) model atmospheres. They found the best fit is a companion with a very dusty atmosphere, $T_{\rm eff} = 1300$ K, and $\log g = 4.4$–4.8, consistent with a late-L spectral type. They also found that the companion alone cannot be responsible for the shape of the inner edge of the debris disk, and suggested there may be additional, unseen lower-mass companions in the system.

Grandjean et al. (2019) combined radial velocity, direct-imaging and astrometry data to place limits on the properties of HD 206893 B. In addition to new constraints on the brown

[9] NHFP Sagan Fellow.
[10] 51 Pegasi b Fellow.
[11] F.R.S.-FNRS Research Associate.

dwarf, they observed a radial velocity drift which was inconsistent with the brown dwarf at its projected separation of ∼11 au. They suggested that an additional inner (1.4–2.6 au), massive (∼15 $M_{\rm Jup}$) companion could explain the radial velocity drift. Both of these companions are internal to the debris disk, which has an inner edge of ∼50 au (Milli et al. 2017).

Stolker et al. (2020) performed the first photometric analysis of the brown dwarf in the M' band with the NACO instrument at the VLT. They found that using a H–L' color–magnitude diagram, the brown dwarf appears less red and consistent with low-gravity objects. However, the brown dwarf appears very red on the L'–M' color–magnitude diagram, inconsistent with field dwarfs by 2σ. They suggested the very red color of the brown dwarf is likely due to enhanced cloud density in the atmosphere, or circumplanetary material.

Ward-Duong et al. (2021) obtained spectra on the brown dwarf with the Gemini Planet Imager (GPI) in J, H, $K1$, and $K2$. The shape of the spectra implied low surface gravity. They found that fitting models to the individual bands produced more internally consistent fits than fitting across the full spectral coverage. The analysis from Stolker et al. (2020) and Ward-Duong et al. (2021) confirmed that the brown dwarf is redder than other field dwarfs with similar spectral types. Using Atacama Large Millimeter/submillimeter Array (ALMA) data, Marino et al. (2020) found that the debris disk surrounding the host HD 206893, external to the brown dwarf, is comprised of two spatially separated belts of dust.

In this work, we present our detection of HD 206893 B in the *Ms* band with the vortex coronagraph on the NIRC2 instrument on Keck. In Section 2 we discuss the *Ms*-band NIRC2 observations and data reduction. In Section 3 we discuss the photometry and astrometry of the companion.

2. Observations and Data Reduction

HD 206893 was observed on UT 2018 September 24 in the *Ms* band (4.670 μm) with the NIRC2 instrument on the Keck telescope. Data were obtained with the vortex coronagraph (Serabyn et al. 2017) in order to minimize the flux from the primary star. Each frame had an exposure time of 0.5 s with 60 coadds for a total of 90 frames and 2700 s total exposure time. Before each set of 25 science frames, three calibration frames were taken. These calibration frames include a sky frame for the science data, an image of the unobscured star at a shorter integration time (0.01 s) to be used as a point-spread function (PSF) reference, and a sky frame for that PSF reference. Data were obtained as part of an ongoing survey targeting stars with debris disks searching for giant planets with deep NIRC2 observations (PI Mawet).

Observations were taken in the vertical-angle mode in order to allow angular differential imaging (ADI; Marois et al. 2006), which provides speckle diversity to be used in postprocessing algorithms. 47° of field rotation was achieved between the first and last frame. Data were obtained in very good seeing conditions, with an average differential image motion monitor (DIMM) of 0.″5.

The quadrant analysis of coronagraphic images for tip-tilt sensing (Huby et al. 2017) was used to keep the primary star well centered behind the vortex coronagraph to minimize stellar-flux leakage into the image.

Data were processed using the NIRC2 preprocessing pipeline,[12] which has been designed specifically to do preprocessing

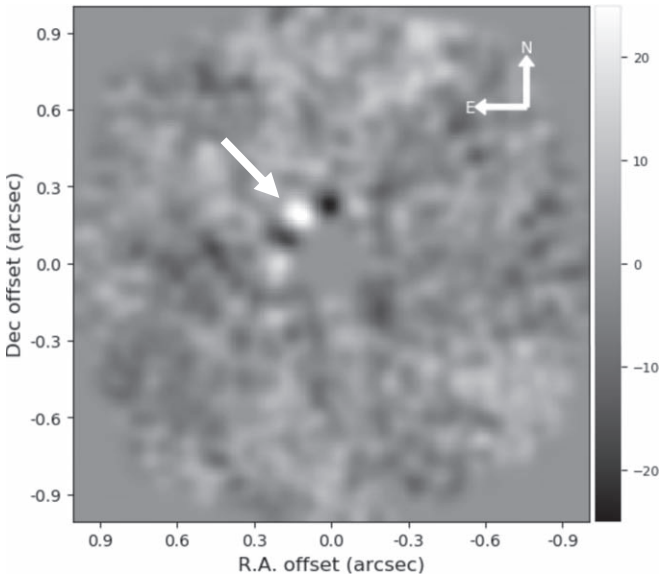

Figure 1. Detection image of HD 206893 B in the *Ms* band using the vortex coronagraph on NIRC2/Keck. The brown dwarf is northeast of the primary star indicated by the white arrow. The image has been smoothed by an FWHM-sized kernel. The image is on a linear scale in counts. The dark lobes around the brown dwarf are artifacts due to the ADI postprocessing due to self-subtraction.

on NIRC2 vortex data. First the frames are centered to the vortex position. The sky frames are subtracted from both the science and PSF reference data. The frames are then corrected for flat-fielding effects and bad pixels. Finally, the frames are recentered based on the speckle locations, as the star is never perfectly centered behind the coronagraph in each frame. The distortion is corrected using the NIRC2 solution (Service et al. 2016), with the pixel scale of $0.009942'' \pm 0.00005''$ pixel^{-1}.

In order to optimally subtract the stellar PSF to reveal the brown-dwarf companion, we use the Vortex Image Processing (VIP; Gomez Gonzalez et al. 2017) package. The VIP package is used after the data are preprocessed with the NIRC2 pipeline. We use the principal component analysis (Amara & Quanz 2012; Soummer et al. 2012) algorithm within VIP which calculates the optimal number of principal components to maximize the signal-to-noise of a point source at a specified location. The optimal number of components for our data is four principal components. Due to uncertainty in the exact position of the host star behind the coronagraph, we perform a grid search of small subpixel-to-pixel shifts of the center of the star and optimize the star center where the brown-dwarf signal-to-noise is maximized. The brown dwarf is clearly detected with a signal-to-noise of 11 to the northeast of the star (Figure 1). The signal-to-noise includes small sample statistics (Mawet et al. 2014) to take into account the smaller number of resolution elements at small separation angles. The image has been smoothed with a kernel the size of the FWHM to emphasize point sources, since the *Ms*-band data is over-sampled. We do not detect any additional companions in the system. The potential inner companion inferred from radial velocity drift by Grandjean et al. (2019) is inside our inner working angle at the suggested separation (∼50 mas).

To extract the astrometry and photometry of the brown dwarf, we inject a fake negative companion at an initial approximate location, and use the downhill simplex method to determine the position and flux that minimize the residuals in the final image. The position and flux is adjusted within a

[12] https://github.com/vortex-exoplanet/NIRC2_Preprocessing

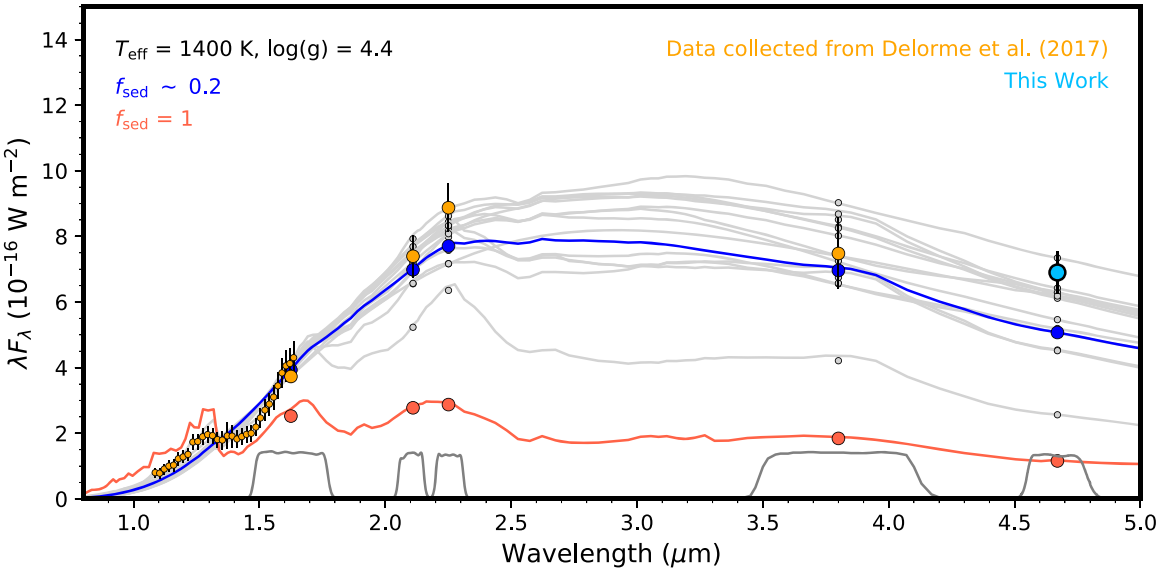

Figure 2. Flux measurements of HD 206893 B across the near-infrared. The orange points are data presented in Delorme et al. (2017), while the light-blue point is our *Ms*-band observation. Each gray curve shows the best-fit model for each set of $T_{\rm eff}$ and log(g) in our model grid, all with $f_{\rm sed} \sim 0.2$. As an example, the dark-blue curve shows the model spectrum for the $T_{\rm eff} = 1400$ K, log(g) = 4.4 case, while the red curve is the corresponding $f_{\rm sed} = 1$ case. $f_{\rm sed} \sim 0.2$ models result in a better fit to the data. The gray, red, and dark-blue points on the model spectra are the band-integrated model fluxes in each filter.

predetermined range and the values which minimize chi-squared are the astrometry and photometry. In order to measure the error on these measurements, we inject a fake companion at six different positions with known radii, position angles, and flux in the data, where the brown dwarf has been subtracted away using the position and flux determined above.

We find that the brown dwarf has an $Ms = 12.97^{0.10}_{-0.11}$, an angular separation of $0\farcs22 \pm 0\farcs03$, and a position angle (PA) of $39.6° \pm 5.4°$ east of north. This is consistent with photometry and astrometry data of the companion in the *M*-band from Stolker et al. (2020), which were also obtained in 2018.

3. Analysis

3.1. Companion Mass from Ms-band Contrast

We estimate the mass of the companion using the average mass from three evolutionary and atmospheric models (Chabrier et al. 2000; Baraffe et al. 2003; Allard et al. 2013) to be 12–78 $M_{\rm Jup}$. We use our *Ms*-band contrast, assume a distance of 40.77 pc (Gaia Collaboration 2020), and an age range of 250^{+450}_{-200} Myr from Delorme et al. (2017). Our mass range is consistent with the Milli et al. (2017) mass range (24–73 $M_{\rm Jup}$), though it extends to lower masses as the age range in Delorme et al. (2017) is lower. The lower end of our mass range, which uses our *Ms*-band contrast measurement alone, is consistent with the mass-estimate ranges from Delorme et al. (2017) (15–30 $M_{\rm Jup}$) and Ward-Duong et al. (2021) (12–40 $M_{\rm Jup}$) from fitting to evolutionary models.

3.2. Atmospheric Properties

We convert the *Ms*-band detection into flux using the Keck NIRC2 *Ms* filter zero-point[13] (Rodrigo et al. 2012; Rodrigo & Solano 2020) and find $\lambda F_\lambda = 6.9^{+0.6}_{-0.7} \times 10^{-16}$ W m^{-2}. We analyze the atmospheric properties of the companion by comparing its SED from 1–5 μm (Milli et al. 2017; Delorme et al. 2017) to a custom grid of models computed using a 1D thermal-structure code to simulate brown-dwarf and exoplanet atmospheres (McKay et al. 1989; Marley et al. 1996; Marley & McKay 1999; Fortney et al. 2005, 2008; Saumon & Marley 2008; Morley et al. 2012). The atmospheric thermal structure and composition are assumed to be in a radiative–convective–thermochemical equilibrium. Clouds are computed self-consistently with the thermal structure using the framework of Ackerman & Marley (2001), with its vertical and particle size distribution controlled by the sedimentation efficiency parameter, $f_{\rm sed}$; a larger $f_{\rm sed}$ results in flattened clouds made of larger particles, while a smaller $f_{\rm sed}$ results in more vertically extended clouds made of smaller particles. Vertical mixing of cloud particles is parameterized through eddy diffusion, with the eddy diffusion coefficient, K_{zz}, computed using mixing-length theory with a minimum internal flux assumed in the radiative part of the atmosphere (Ackerman & Marley 2001).

We explore ranges of $T_{\rm eff}$ from 1200–1600 K in 100 K steps and log(g) = 4.0, 4.4, and 5.0, and consider forsterite and iron clouds. This grid covers the parameter space of the best-fitting Exo-REM models from Delorme et al. (2017) and extends beyond it to higher and lower temperatures, and lower gravities. We first try to reproduce the Exo-REM model spectra, as they include a treatment of the Ackerman & Marley (2001) cloud parameterization (Charnay et al. 2018). However, we found that setting $f_{\rm sed} = 1$, as was done for the Exo-REM models in Delorme et al. (2017), does not result in the same model spectra nor a good fit to the data (red curve in Figure 2). This could be due to model differences in K_{zz} parameterization and how it responds to cloud radiative feedback. The inclusion of clouds tends to increase mixing, and thus K_{zz}, within the cloud due to increased opacity, which leads to a negative feedback effect of decreasing cloud opacity for a fixed $f_{\rm sed}$. While our model self-consistently computes K_{zz} with the thermal structure, Exo-REM does not (B. Charnay 2021,

[13] https://svo.cab.inta-csic.es/main/index.php

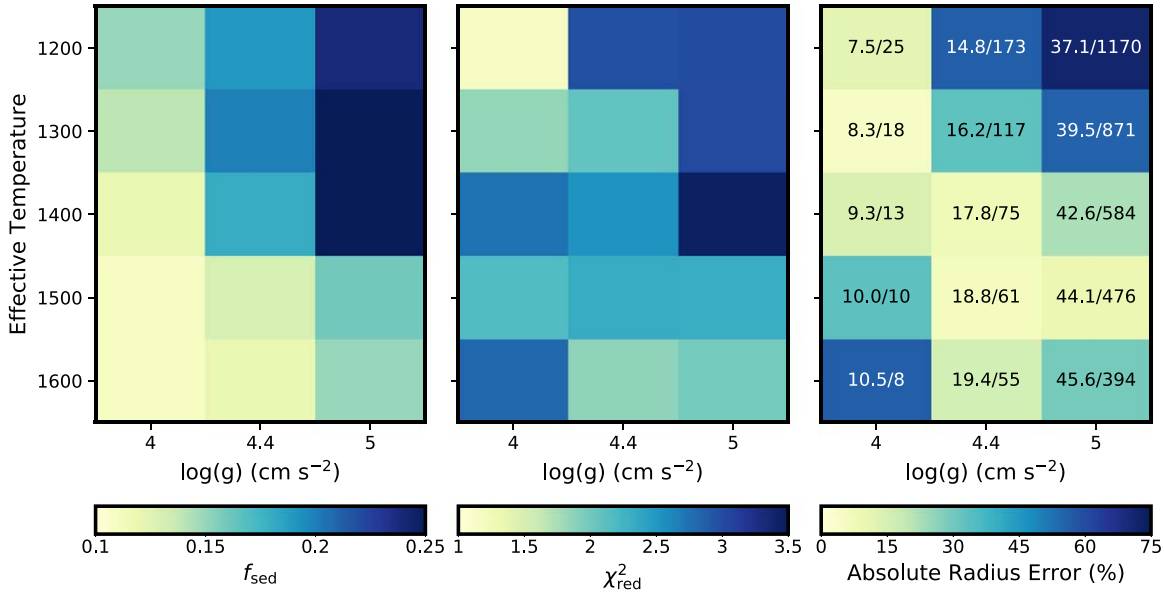

Figure 3. The f_{sed} (left), reduced chi-square (middle), and absolute radius error (Equation (1)) between the retrieved radii and those predicted by the evolutionary model of Saumon & Marley (2008) (right) for the grid of models we tested. The mass/age of each evolutionary model, in units of M_{Jup}/Myr, are indicated for each model in the radius error plot.

personal communication), which may explain our lower cloud opacity.

We find that f_{sed} values $\sim$0.2 are needed to best fit our model to the data (blue curve in Figure 2; Figure 3, left), a much lower value than those considered in Delorme et al. (2017), indicating highly vertically extended clouds. In addition, the best-fit f_{sed} decreases to $\sim$0.1 toward higher temperatures and lower gravities, likely due to the increased atmospheric temperatures leading to lower cloud masses, resulting in the need for more vertically extended clouds to replicate the same observed reddening. Such low f_{sed} values are unusual for substellar objects, which typically possess $f_{sed} \geqslant 1$ when fit with our thermal-structure model (e.g., Stephens et al. 2009; Marley et al. 2012; Morley et al. 2012; Rajan et al. 2017). On the other hand, it could be evidence for a population of small, high-altitude grains that appear to "extend" a more typical set of iron/forsterite cloud layers (Hiranaka et al. 2016). Delorme et al. (2017) and Ward-Duong et al. (2021) both showed that extinction due to submicron forsterite particles in the brown dwarf's atmosphere could lead to sufficient reddening of its emission spectrum to explain the observations, though they did not take into account the feedback between the submicron particles and the atmosphere. A possible source of these submicron particles is that the brown dwarf may be accreting dust from the debris belt, populating the atmosphere with small, high-altitude grains (Marino et al. 2020; Ward-Duong et al. 2021). In Section 3.4 we show that the brown dwarf is likely responsible for stirring the planetesimals in the debris disk, lending some strength to this scenario. Delorme et al. (2017) and Stolker et al. (2020) suggested there may be a circumplanetary disk around HD 206893 B (similar to predictions around the red companion G 196-3 B Zakhozhay et al. 2017) though recent ALMA observations of the system by Marino et al. (2020) showed no dust around the brown dwarf, with a dust upper limit of $2 \times 10^{-4}\,M_{\oplus}$.

We are not able to reproduce the water absorption feature at 1.4 μm, as the atmosphere becomes similar to a blackbody due to the low pressures at the photosphere. This sets a lower limit to the reduced χ^2 of most of our model fits to $\sim$2 (Figure 3). Interestingly, the $T_{\rm eff} = 1200$ K and $\log(g) = 4$ model does show a hint of the water feature, resulting in a reduced χ^2 of nearly 1. However, the resulting implications for the companion's mass and age (see Section 3.3) render this result suspect. Instead, we could be seeing numerical instabilities in the cloud treatment at these extreme f_{sed} values. Our results are in contrast with those of Delorme et al. (2017), who were able to reproduce the water feature. Though our $f_{sed} = 1$ models are able to do the same, they are far too dim at longer wavelengths. One possible solution is inhomogeneity in the cloud cover (Marley et al. 2010; Lew et al. 2016), though it would require the remaining clouds to be even more optically thick/vertically extended to maintain the extreme redness. In addition, Ward-Duong et al. (2021) observed a drop in flux beyond 2.3 μm with K2 spectra. Our models are not able to reproduce this significant near-infrared feature alongside the high *L*- and *Ms*-band fluxes, suggesting that we could be missing important details in our model, such as absorption longward of 2.3 μm and/or cloud physics that is not captured by the Ackerman & Marley (2001) models.

3.3. Evolutionary Models

We compare our best-fit radii for the companion to evolutionary models (Saumon & Marley 2008) to differentiate between the different $T_{\rm eff}$ and $\log(g)$ cases and to estimate the companion's age and mass. We define an absolute radius error between our best-fit radii $R_{\rm fit}$ and those predicted by the evolutionary models, $R_{\rm evo}$, as

$$\text{Absolute Radius Error} = \frac{|R_{\rm evo} - R_{\rm fit}|}{R_{\rm evo}}. \quad (1)$$

We find that there are multiple models with $R_{\rm fit}$ and $R_{\rm evo}$ differing by $<$10%, though in general models that are either cool and low gravity or warmer and higher gravity are preferred (Figure 3). These models in turn imply masses $<$20 $M_{\rm Jup}$ and

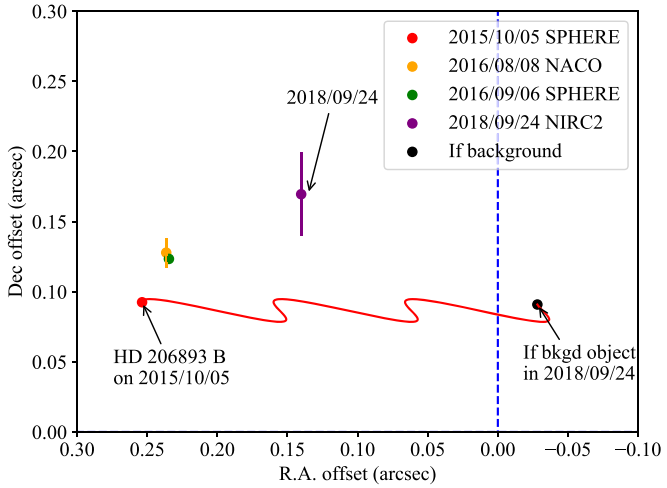

Figure 4. Position of the brown dwarf relative to its host star since 2015. Error bars are included on the plot, though they are small and most are encompassed inside the points.

ages <100 Myr, within the range derived by Delorme et al. (2017) and consistent with the mass-estimate range from our *Ms*-band measurement in Section 3.1 (12–78 $M_{\rm Jup}$). It is also consistent with the lower mass estimate in Ward-Duong et al. (2021) due to the peak-shaped morphology of the *H*-band spectra. However, we note that the evolutionary models to which we have compared were not computed for such red objects (Saumon & Marley 2008), so age and mass estimates stemming from such comparisons may not be reliable. For the subsequent analysis, we take the conservative approach and use our derived mass range from Section 3.1 (12–78 $M_{\rm Jup}$).

3.4. Astrometry

The clear *Ms*-band detection shows significant orbital motion compared to the data presented in the discovery paper (Milli et al. 2017). Figure 4 shows the position of the brown dwarf relative to the host star over several years since the discovery in 2015. The black point indicates the position that the 2015-detected point source would be if it were a background star, using parallax and the proper motion of HD 206893. We show that our 2018 *Ms*-band Keck/NIRC2 detection is not consistent with a background star and its movement is likely orbital motion.

In order to put constraints on the detected orbital motion, we input the separation and PA values from Table 1 into the *orbitize* python package (Foreman-Mackey et al. 2013; Blunt et al. 2020). We assume a stellar mass of $1.32 \pm 0.02\,M_{\odot}$ (Delorme et al. 2017) and the brown-dwarf mass range derived in this work (12–78 $M_{\rm Jup}$). This is a total system mass of $1.36 \pm 0.04\,M_{\odot}$. We assume a parallax of 24.53 ± 0.04 mas (Gaia EDR3). We fit the orbit using Markov Chain Monte Carlo with 20 temperatures, 100 walkers, 10^6 orbits, and 10^5 burn steps.

The derived orbital parameters are presented in Table 2. The posterior distributions are shown in the Appendix (see Figure 6). We find that the brown dwarf has a semimajor axis of $10.46^{+1.47}_{-1.93}$ au. This is consistent with the semimajor axes estimated by Milli et al. (2017), Delorme et al. (2017), Stolker et al. (2020), and Ward-Duong et al. (2021). The eccentricity derived in Marino et al. (2020) is consistent with our eccentricity range of $0.22^{+0.16}_{-0.16}$.

HD 206893 B is located inside the observed debris belts (Milli et al. 2017; Marino et al. 2020). HD 206893 B is sufficiently far away from the debris belt so that its chaotic zone does not overlap with the belt (vertical gray box in Figure 5), calculated assuming the chaotic zone's inner edge $(1–1.17\mu^{0.28})a_{\rm pl}$ and the outer edge $(1 + 1.76\mu^{0.31})a_{\rm pl}$ where μ is the mass ratio between the brown dwarf and the star, and $a_{\rm pl}$ is the semimajor axis of the planet (see Morrison & Malhotra 2015, their Table 1). For the brown dwarf's mass, we assume the mass range 12–78 $M_{\rm Jup}$ derived in this work in Section 3.1. The wide chaotic zone also suggests a wide cavity around the orbit of the brown dwarf between ∼2.4 and ∼18.5 au.

Next, we assess whether the observed debris belt is stirred by HD 206893 B. The debris belt could potentially be maintained by self-stirring, i.e., the collision of ∼1000 km sized bodies at the top of the collisional cascade. Using Krivov & Booth (2018), we estimate the self-stirring timescale to be:

$$t_{{\rm ss},i} \sim 3.8\ {\rm Myr}\left(\frac{1.24\,M_{\odot}}{M_{\star}}\right)^{0.35} \times \left(\frac{a_{\rm disk}}{28\ {\rm au}}\right)^{3.575}\left(\frac{\Delta a/a_{\rm disk}}{0.73}\right)^{1.15} \quad (2)$$

Table 1
Astrometry of HD 206893 B

Observation Dates (UT)	Instrument	Separation (mas)	PA (°)
2015 Oct 4[a]	SPHERE/VLT	270.4 ± 2.6	69.95 ± 0.55
2016 Aug 8[a]	NACO/VLT	268.8 ± 10.4	61.6 ± 1.9
2016 Sep 16[b]	SPHERE/VLT	265 ± 2	62.25 ± 0.11
2016 Sep 22[c]	GPI/Gemini	267.6 ± 2.9	62.72 ± 0.62
2016 Oct 21[c]	GPI/Gemini	265.0 ± 2.7	61.33 ± 0.64
2017 Jul 14[d]	SPHERE/VLT	260.3 ± 2	54.2 ± 0.4
2017 Nov 09[c]	GPI/Gemini	256.9 ± 1.1	51.01 ± 0.35
2018 Jun 20[d]	SPHERE/VLT	249.1 ± 1.6	45.5 ± 0.4
2018 Jun 8[e]	NACO/VLT	246.51 ± 21.34	42.80 ± 2.24
2018 Sep 24[c]	GPI/Gemini	251.7 ± 5.4	42.6 ± 1.6
2018 Sep 24[f]	NIRC2/Keck	220 ± 30	39.6 ± 5.4

Notes.
[a] Milli et al. (2017).
[b] Delorme et al. (2017).
[c] Ward-Duong et al. (2021).
[d] Grandjean et al. (2019).
[e] Stolker et al. (2020).
[f] This work.

Table 2
Orbital Parameters of HD 206893 B

Parameter	Posterior 50% ± 1 σ	Unit
Semimajor axis (*a*)	$10.46^{+1.47}_{-1.93}$	au
Eccentricity (*e*)	$0.22^{+0.16}_{-0.16}$	⋯
Inclination (*i*)	$143.21^{+14.99}_{-5.93}$	°
Argument of periastron (ω)	$177.3^{+111.8}_{-130.1}$	°
Position angle of nodes (Ω)	$152.3^{+111.1}_{-88.0}$	°
Epoch of periastron passage (τ)	$0.28^{+0.44}_{-0.12}$	⋯

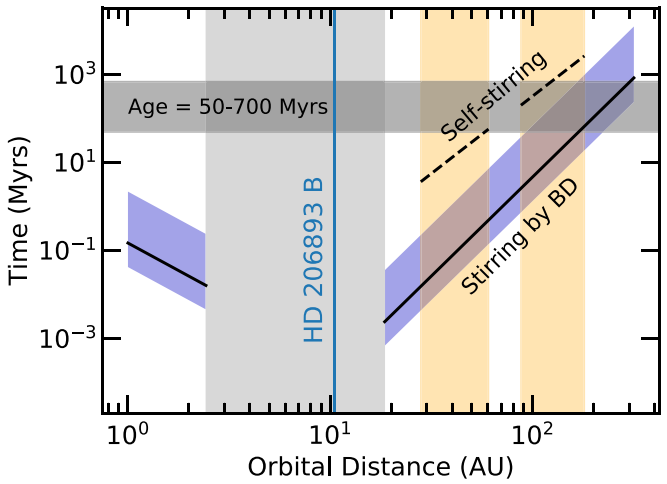

Figure 5. The timescale for HD 206893 B to stir particles at different orbital distances. The thick vertical gray box illustrates the chaotic zone around the orbit of HD 206893 B given the range of masses 12–78 $M_{\rm Jup}$. The orange boxes show the reported width and location of the debris belts (Marino et al. 2020). The horizontal gray line shows the age range of the brown dwarf. The dashed line shows the self-stirring scenario, where the dust is maintained by self-stirring by the planetesimals. The solid black line is the scenario where stirring by the brown dwarf dominates, with a blue outline to indicate the range in both masses and eccentricities (0.22 ± 0.16) of HD 206893 B. Due to the position and relatively high mass of the brown dwarf, the collisions in the debris belt are likely maintained by secular perturbations from HD 206893 B.

for the inner belt, and

$$t_{\rm ss,o} \sim 2.9\ {\rm Gyrs}\left(\frac{1.24\ M_\odot}{M_\star}\right)^{0.35} \times \left(\frac{a_{\rm disk}}{180\ {\rm au}}\right)^{3.575}\left(\frac{\Delta a/a_{\rm disk}}{0.69}\right)^{1.15} \quad (3)$$

for the outer belt, where $a_{\rm disk}$ is the semimajor axis of the planetesimals, $M_\star$ is the mass of the host star, and Δa is the width of the debris belts, taken from Marino et al. (2020). Figure 5 demonstrates that the inner belt could be maintained by self-stirring but in the outer belt, $t_{\rm ss}$ is comparable to the age of the system. We note however that if these 1000 km sized bodies can be coagulated before the dispersal of the disk gas, the self-stirring timescale can be dramatically shortened (e.g., Krivov & Booth 2018).

We now consider stirring of the debris belt from secular perturbation by HD 206893 B. The orbit-crossing timescale of two planetesimals as their eccentricities are pumped by the brown dwarf can be approximated as $t_{\rm cross} \sim 1/Ae_{\rm bd}$ where A is the precession frequency and $e_{\rm bd}$ is the eccentricity of the brown dwarf. We follow Mustill & Wyatt (2009) to compute $t_{\rm cross}$ for particles that are interior and exterior to the brown dwarf, assuming particles were initially on circular orbits:

$$t_{\rm cross} \approx 2.8\ {\rm Myr}\ \frac{(1-e_{\rm bd}^2)^{3/2}}{e_{\rm bd}}\left(\frac{a_{\rm disk}}{100\ {\rm au}}\right)^{9/2} \times \left(\frac{M_\star}{M_\odot}\right)^{1/2}\left(\frac{16\ M_{\rm Jup}}{M_{\rm bd}}\right)\left(\frac{10.6\ {\rm au}}{a_{\rm bd}}\right)^3 \quad (4)$$

for particles exterior to the brown dwarf's orbit, and

$$t_{\rm cross} \approx 91\ {\rm kyr}\ \frac{(1-e_{\rm bd}^2)^{3/2}}{e_{\rm bd}}\left(\frac{a_{\rm bd}}{10.6\ {\rm au}}\right)^4 \times \left(\frac{M_\star}{M_\odot}\right)^{1/2}\left(\frac{16\ M_{\rm Jup}}{M_{\rm bd}}\right)\left(\frac{1\ {\rm au}}{a_{\rm disk}}\right)^{5/2} \quad (5)$$

for particles interior to the brown dwarf's orbit, where the subscript "bd" corresponds to the brown dwarf. The large mass of HD 206893 B drives $t_{\rm cross}$ at least two orders of magnitude shorter than $t_{\rm ss}$, suggesting the observed debris belt is likely shaped by the brown dwarf. Even after accounting for the uncertainties in both mass and eccentricity of the brown dwarf, its secular perturbation dominates over self-stirring (see the blue band in Figure 5). We note that the actual mass of the debris belt is not well constrained since the mass is dominated by large planetesimals (i.e., at the top of the collisional cascade) that are invisible. If the belt is more massive than the minimum mass solar nebula by at least two orders of magnitude, self-stirring can play a dominant role in replenishing the belt. There are reports of additional companions in the system including one massive companion interior to HD 206893 B (Grandjean et al. 2019) and another putative Jupiter-mass planet carving out the debris gap (Marino et al. 2020). We note that the innermost companion, despite its mass, is too far away from the debris to have played a dominant role in sculpting the belts (the orbit-crossing timescale within the belts due to the secular perturbation by the innermost companion is ~4 orders of magnitude longer than that by HD 206893 B calculated using 2.6 au, 15 $M_{\rm Jup}$, and $e = 0.02$). The putative Jupiter-mass planet inside the gap is more likely to be stirring the belts. Assuming $e = 0.02$, 0.9 $M_{\rm Jup}$, and 74 au, the orbit-crossing timescale is just as short as that due to HD 206893 B, but only for the outer belt. For this gap-opening planet to be a major stirrer of the inner belt, its eccentricity needs to be higher than ~0.2. Our estimates are consistent with the analysis of Marino et al. (2020); see their Figure 10.

4. Conclusions

We detected the brown dwarf HD 206893 B in the *Ms* band with the Keck NIRC2 instrument and the vortex coronagraph (Serabyn et al. 2017) on 2018 September 24 with a signal-to-noise of 11. We measure its magnitude to be $Ms = 12.97^{0.10}_{-0.11}$ and find its position is at an angular separation of $0\farcs22 \pm 0\farcs03$, and a position angle of $39.6° \pm 5.4°$ east of north. We use three evolutionary and atmospheric models (Chabrier et al. 2000; Baraffe et al. 2003; Allard et al. 2013), and assume a distance of 40.77 pc (Gaia Collaboration 2020) and an age of 250^{+450}_{-200} Myr (Delorme et al. 2017) to estimate the mass to be 12–78 $M_{\rm Jup}$. We analyze the atmospheric properties of the brown dwarf from 1–5 μm using a grid of models appropriate to simulate brown dwarfs and exoplanet atmospheres (McKay et al. 1989; Marley et al. 1996; Marley & McKay 1999; Fortney et al. 2005, 2008; Saumon & Marley 2008; Morley et al. 2012). We find that an $f_{\rm sed}$ value ~0.2 provides the best fit to the data, suggesting high vertically extended clouds. This may be indicative of high-altitude grains or a circumplanetary disk. We use evolutionary models

(Saumon & Marley 2008) to find the best-fitting masses and ages are $<20\ M_{\rm Jup}$ and ages <100 Myr, respectively. This is similar to the range derived by Delorme et al. (2017) and consistent with our estimates from the *Ms*-band photometry alone. We detect orbital motion of the brown dwarf around the host star in our 2018 data compared to the original 2015 and 2016 data (Delorme et al. 2017; Milli et al. 2017). We derive orbital parameters for the brown dwarf using the *orbitize* python package (Foreman-Mackey et al. 2013; Blunt et al. 2020). Finally we estimate the width of the chaotic zone of the brown-dwarf companion in order to analyze how it interacts with the debris belt. We find that, due to the position and large mass of HD 206893 B, the debris belt is likely stirred by secular perturbation from the brown dwarf, rather than self-stirring of the planetesimals.

We thank the anonymous referee for their helpful suggestions that improved this paper. We thank our Keck/NIRC2 support staff, without whom the data could not have been obtained: Cynthia, Terry Stickel, Greg Doppmann, Bruno Femenía Castellá, and Carlos Alvarez. P.G. and J.W. acknowledge support from the 51 Pegasi b Fellowship sponsored by the Heising-Simons Foundation. P.G. is also supported by NASA through the NASA Hubble Fellowship grant HST-HF2-51456.001-A awarded by the Space Telescope Science Institute, which is operated by the Association of Universities for Research in Astronomy, Inc., for NASA, under contract NAS5-26555. Part of this work has received funding from the European Research Council (ERC) under the European Union's Horizon 2020 research and innovation program (grant agreement No. 819155). This research has made use of the SVO Filter Profile Service (http://svo2.cab.inta-csic.es/theory/fps/) supported from the Spanish MINECO through grant AYA2017-84089. The plots presented in this paper we created using matplotlib in python (Hunter 2007). The data presented herein were obtained at the W.M. Keck Observatory, which is operated as a scientific partnership among the California Institute of Technology, the University of California and NASA. The Observatory was made possible by the generous financial support of the W.M. Keck Foundation. The authors wish to recognize and acknowledge the very significant cultural role and reverence that the summit of Maunakea has always had within the indigenous Hawaiian community. We are most fortunate to have the opportunity to conduct observations from this mountain.

Appendix

Figure 6 shows the posterior distributions for the derived orbital parameters for HD 206893 B using the *orbitize* python package.

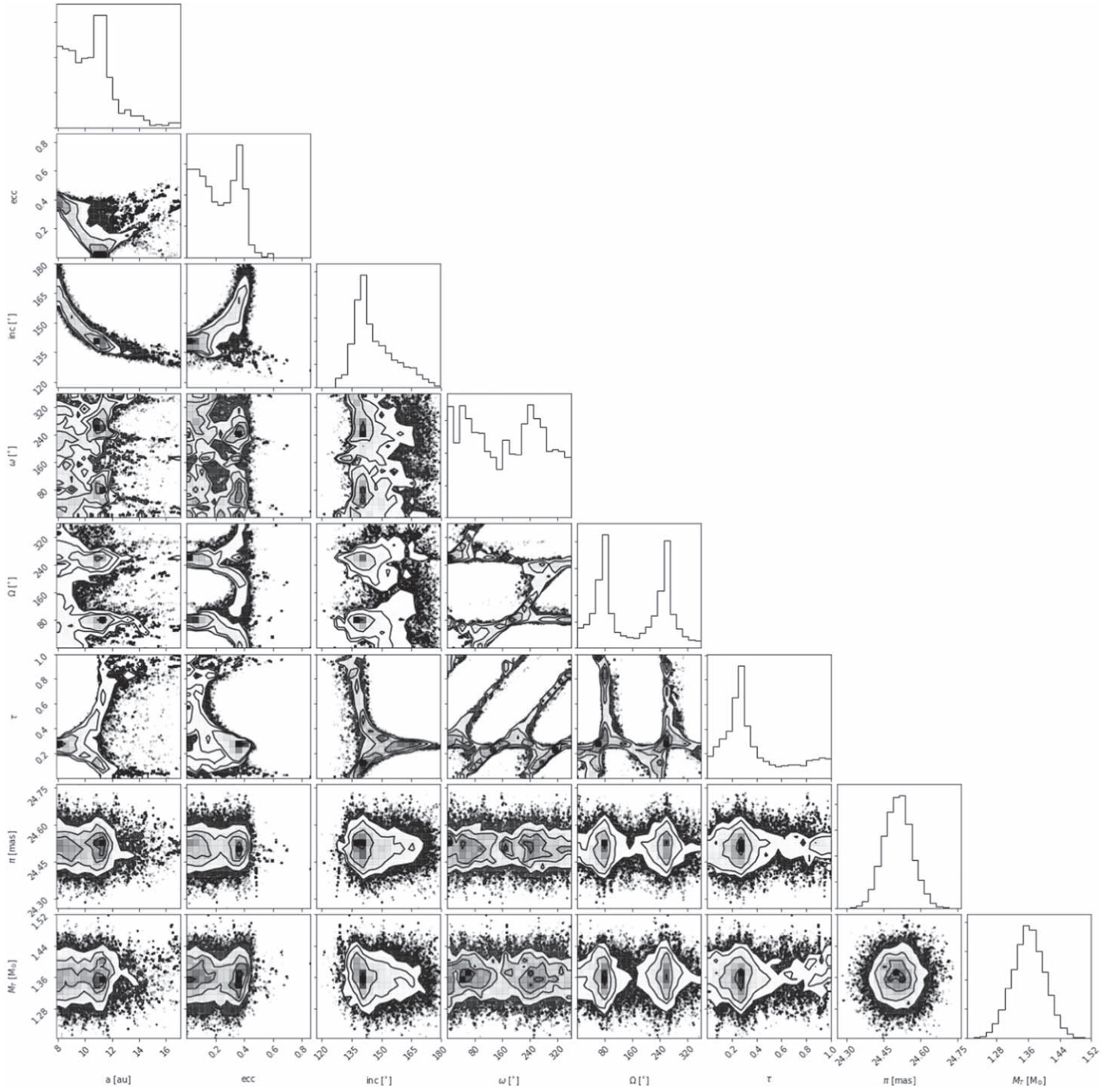

Figure 6. Posterior distributions for the orbital fit solution for HD 206893 B. The orbital parameters were derived using published astrometry (Delorme et al. 2017; Milli et al. 2017; Grandjean et al. 2019; Stolker et al. 2020; Ward-Duong et al. 2021) as well as the values derived in this work.

ORCID iDs

Tiffany Meshkat https://orcid.org/0000-0001-6126-2467
Peter Gao https://orcid.org/0000-0002-8518-9601
Eve J. Lee https://orcid.org/0000-0002-1228-9820
Dimitri Mawet https://orcid.org/0000-0002-8895-4735
Elodie Choquet https://orcid.org/0000-0002-9173-0740
Marie Ygouf https://orcid.org/0000-0001-7591-2731
Rahul Patel https://orcid.org/0000-0002-5025-6827
Garreth Ruane https://orcid.org/0000-0003-4769-1665
Jason Wang https://orcid.org/0000-0003-0774-6502
Nicole Wallack https://orcid.org/0000-0003-0354-0187
Olivier Absil https://orcid.org/0000-0002-4006-6237

References

Ackerman, A. S., & Marley, M. S. 2001, ApJ, 556, 872
Allard, F. 2014, in IAU Symp. 299, Exploring the Formation and Evolution of Planetary Systems, ed. M. Booth, B. C. Matthews, & J. R. Graham (Cambridge: Cambridge Univ. Press), 271
Allard, F., Homeier, D., Freytag, B., et al. 2013, MSAIS, 24, 128
Amara, A., & Quanz, S. P. 2012, MNRAS, 427, 948

Baraffe, I., Chabrier, G., Barman, T. S., Allard, F., & Hauschildt, P. H. 2003, A&A, 402, 701
Baudino, J. L., Bézard, B., Boccaletti, A., et al. 2015, A&A, 582, A83
Blunt, S., Wang, J. J., Angelo, I., et al. 2020, AJ, 159, 89
Chabrier, G., Baraffe, I., Allard, F., & Hauschildt, P. 2000, ApJ, 542, 464
Charnay, B., Bézard, B., Baudino, J. L., et al. 2018, ApJ, 854, 172
David, T. J., Hillenbrand, L. A., Petigura, E. A., et al. 2016, Natur, 534, 658
Delorme, P., Schmidt, T., Bonnefoy, M., et al. 2017, A&A, 608, A79
Foreman-Mackey, D., Hogg, D. W., Lang, D., & Goodman, J. 2013, PASP, 125, 306
Fortney, J. J., Marley, M. S., Lodders, K., Saumon, D., & Freedman, R. 2005, ApJL, 627, L69
Fortney, J. J., Marley, M. S., Saumon, D., & Lodders, K. 2008, ApJ, 683, 1104
Gaia Collaboration 2020, yCat, 1350, 0
Gomez Gonzalez, C. A., Wertz, O., Absil, O., et al. 2017, AJ, 154, 7
Grandjean, A., Lagrange, A. M., Beust, H., et al. 2019, A&A, 627, L9
Hiranaka, K., Cruz, K. L., Douglas, S. T., Marley, M. S., & Baldassare, V. F. 2016, ApJ, 830, 96
Huby, E., Bottom, M., Femenia, B., et al. 2017, A&A, 600, A46
Hunter, J. D. 2007, CSE, 9, 90
Konopacky, Q. M., Rameau, J., Duchêne, G., et al. 2016, ApJL, 829, L4
Krivov, A. V., & Booth, M. 2018, MNRAS, 479, 3300
Lew, B. W. P., Apai, D., Zhou, Y., et al. 2016, ApJL, 829, L32
Marino, S., Zurlo, A., Faramaz, V., et al. 2020, MNRAS, 498, 1319
Marley, M. S., & McKay, C. P. 1999, Icar, 138, 268
Marley, M. S., Saumon, D., Cushing, M., et al. 2012, ApJ, 754, 135
Marley, M. S., Saumon, D., & Goldblatt, C. 2010, ApJL, 723, L117
Marley, M. S., Saumon, D., Guillot, T., et al. 1996, Sci, 272, 1919
Marois, C., Lafrenière, D., Doyon, R., Macintosh, B., & Nadeau, D. 2006, ApJ, 641, 556
Mawet, D., Milli, J., Wahhaj, Z., et al. 2014, ApJ, 792, 97
McKay, C. P., Pollack, J. B., & Courtin, R. 1989, Icar, 80, 23
Milli, J., Hibon, P., Christiaens, V., et al. 2017, A&A, 597, L2
Moór, A., Ábrahám, P., Derekas, A., et al. 2006, ApJ, 644, 525
Morley, C. V., Fortney, J. J., Marley, M. S., et al. 2012, ApJ, 756, 172
Morrison, S., & Malhotra, R. 2015, ApJ, 799, 41
Mustill, A. J., & Wyatt, M. C. 2009, MNRAS, 399, 1403
Rajan, A., Rameau, J., De Rosa, R. J., et al. 2017, AJ, 154, 10
Rodrigo, C., & Solano, E. 2020, in Contributions to the XIV.0 Scientific Meeting (Virtual) of the Spanish Astronomical Society, 182, https://www.sea-astronomia.es/reunion-cientifica-2020
Rodrigo, C., Solano, E., & Bayo, A. 2012, SVO Filter Profile Service Version 1.0, IVOA Working Draft
Saumon, D., & Marley, M. S. 2008, ApJ, 689, 1327
Serabyn, E., Huby, E., Matthews, K., et al. 2017, AJ, 153, 43
Service, M., Lu, J. R., Campbell, R., et al. 2016, PASP, 128, 095004
Soummer, R., Pueyo, L., & Larkin, J. 2012, ApJL, 755, L28
Stephens, D. C., Leggett, S. K., Cushing, M. C., et al. 2009, ApJ, 702, 154
Stolker, T., Quanz, S. P., Todorov, K. O., et al. 2020, A&A, 635, A182
Ward-Duong, K., Patience, J., Follette, K., et al. 2021, AJ, 161, 5
Zakhozhay, O. V., Zapatero Osorio, M. R., Béjar, V. J. S., & Boehler, Y. 2017, MNRAS, 464, 1108
Zuckerman, B., & Song, I. 2004, ApJ, 603, 738